

## 4 Effect of various experimental parameters in laser surface structuring of silicon

**Abstract** – The laser beam parameters influence the characteristics of the surface structures, e.g. shape of crater and fine features. As discussed earlier, number of pulses and energy per pulse have significant role in defining density, arrangement and size of the LIPSSs as well on the decoration of the processed surface with ablated particles. Here, we analyze further how laser beam features like wavelength and pulse repetition rate influence the LIPSS features. The experimental results are compared with some simulation predictions addressing the role of hydrothermal wave character of the grooves formation. In addition, we report on the effect of the ambient pressure.

### 4.1 Introduction

The most common low spatial frequency LIPSS (LSFL) are ripples with near-wavelength period. Ripples have been very much investigated and their formation mechanisms are generally ascribed to the excitation of surface scattered waves, e.g. surface plasmon polaritons (SPPs), or self-organization of surface instabilities [1–3]. However, for the generation of grooves, the other surface structures with supra-wavelength period and orientation parallel to the laser polarization, there is no general explanation yet. Some prediction models [1] and experimental findings [4] suggest a relevant influence of hydrodynamics of molten material and redeposition of ablated particles [1,4–6]. Grooves typically form at high fluence and number of pulses, hence hereafter we will select experimental conditions that favor their creation in order to clarify the influence of the experimental parameters on this less investigated LIPSS. In particular, in this chapter the influence of ambient and laser beam conditions is discussed. The experiments are carried out with standard beams with a Gaussian intensity profile and homogenous polarization. In section 4.2, the influence of the pulse repetition rate (RR) on fs laser irradiation of silicon, in air, is experimentally investigated in the range 10 Hz – 200 kHz. The analysis considers both the features of the shallow craters and the LIPSSs produced inside the crater evidencing interesting effects of the pulse repetition rate. Section 4.3 reports experimental results on an analysis carried out at two different laser wavelengths  $\lambda$ , namely 513 nm and 1026 nm, at fluences above the grooves formation

threshold. Both static and dynamic irradiations conditions are used and the role of number of pulses  $N$  and laser peak fluence  $F_p$  for both wavelengths is discussed. In this section, also the results of simulations carried out in a collaboration with Dr. George D. Tsibidis are shown and compared to the experimental findings. In section 4.4, the variation of ambient pressure and its effect on the morphology of ripples and formation of grooves is highlighted. Moreover, the impact of variation of laser beam polarization in vacuum condition is also investigated.

## 4.2 Effect of laser pulse repetition rate

Direct fs laser surface structuring can be very useful for applications like fast generation of high regular patterns over a large area [7] or for fast laser drilling [8,9]. In such a case high repetition rate laser source are considered and associated to dynamic and static irradiation conditions. Studies on high repetition rate (HRR) ( $\geq 50$  kHz) for both micro-hole drilling and surface texturing show interesting results [10–13], suggesting that repetition rate of pulsed laser beams can open a new degree of freedom to approach the proper temporal separation between pulses during fs laser processing.

In this section, results of an experimental analysis designed to investigate the process of irradiation of a silicon target from low to high repetition rates, in the range 10 Hz – 200 kHz are presented. Features of both crater and fine structures are analyzed as a function of the fs laser pulse repetition rate. The samples were prepared in static irradiation conditions with a fixed number of pulses.

The fs pulses were provided by a chirped pulse amplification Yb:KGW (1030 nm,  $\approx 180$  fs, maximum pulse energy  $\approx 1.5$  mJ), capable of delivering pulses from single shot up to a maximum repetition rate of 200 kHz. The beam was focused on an intrinsic, (100) silicon plate using a lens with a nominal focal length of 200 mm, in air. The target was mounted on a XY-translation stage located perpendicular to the laser beam direction. The morphology of the irradiated surfaces was analyzed by field emission scanning electron microscopy (FE-SEM) for the LSFL structures and by a stylus profilometer (Dektak XT) capable of providing a tridimensional (3D) view of the shallow crater profile.

The laser beam has the Gaussian spatial profile. Therefore, the  $1/e^2$ -beam waist  $w_0$ , which was discussed in detail in Chapter 2, is obtained by employing the following relation:

$$r^2 = \frac{w_0}{2} \ln\left(\frac{E}{E_{th}}\right) \quad (1)$$

where  $r$  is the radius of the crater produced on silicon with laser pulse energy  $E$ , and  $E_{th}$  is the threshold energy for ablation. The size of the craters generated by  $N = 200$  number of pulses, using lower RRs of 10 Hz and 1 kHz are well fitted to Equation (1) and gives the values of  $w_0 = (35 \pm 1) \mu\text{m}$ , and  $E_{th} = (2.6 \pm 0.4) \mu\text{J}$ . The dependence at high repetition rates of 20 and 200 kHz shows some changes [14], as illustrated later.

Figure 4.1 shows the variation of the crater radius with RR; the values are normalized to the crater size at 10 Hz. We can observe two regimes of low and high RRs with a clear transition occurring for RR around 10 kHz. For HRR irradiation, two effects can influence the process: heat accumulation and ablation plume shielding. Heat accumulation occurs when the fraction of energy released to the target in form of heat cannot diffuse out because the temporal separation between consecutive pulses is too short [11,13,15,16].

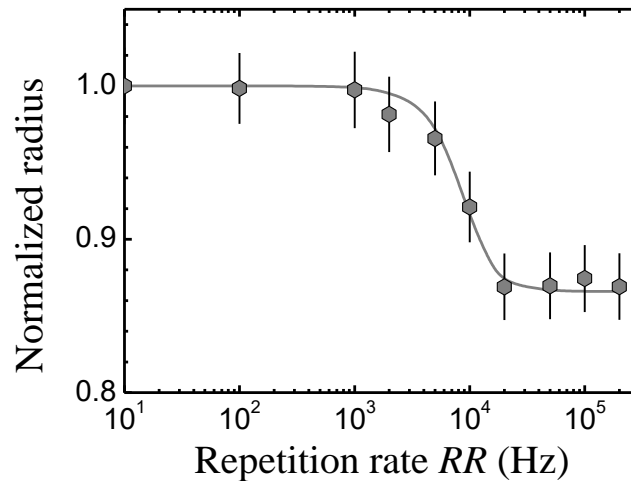


Figure 4.1 Crater radius dependence on the repetition rate RR, at  $E = 10 \mu\text{J}$  and  $N = 200$  pulses. The data points are normalized to the value of the crater radius at 10 Hz. The line is a guide to the eye [14].

Pulse after pulse, an increase of the target temperature occurs, and transport of energy out of the irradiated region can cause irreversible changes, and surface damage in the surroundings of the irradiated area. This effect has been typically observed for values of several hundred kHz, or MHz, and is expected to become important for silicon at RRs of several MHz or more [17]. In such cases, larger craters with rougher shapes are also observed due to heat diffusion and accumulation [11,16]. Moreover, the effect increases at higher RRs. In our case, however, we observe a similar trend of the crater size for 20 kHz and 200 kHz [14] and a reduction of the crater size with respect to that obtained at low RR. This suggests that heat accumulation should play a minor role in our experimental conditions.

In ablative conditions, the second effect that can influence the process, i.e., plume shielding, takes place when the residence time of the cloud of ablated particles above the target surface is comparable with the pulse separation. Ultrashort laser ablation of a solid target results in the emission of an atomic plasma plume consisting of electrons, atoms and ions followed, on a longer timescale, by a cloud of nanoparticles, which typically accounts for the largest part of the ablated volume [18–21]. The pulse separation in multi-pulse laser irradiation at high repetition rate is large enough and involves the interaction with the ablated material at a longer delay after the pulse. The typical expansion time of a fs laser ablation nanoparticles plume in a vacuum is of several tens of  $\mu\text{s}$ , and its residence time over the target surface becomes even larger in a background gas, due to confinement effects [14].

The craters of SEM images in Figure 4.2 are produced by irradiation sequences of  $N = 200$  laser pulses at a pulse energy  $E = 10 \mu\text{J}$  for different values of the repetition rates. Panels (a) and (e) shows the reduction in size of the ablated crater at 200 kHz compared to that of 10 Hz. The observed reduction of the crater size can be reasonably ascribed to a plume shielding effect that induces a reduction of the effective energy reaching the target surface, due to absorption and scattering of the laser light by the ablated material close to the target surface at these values of the RRs [14]. Plume shielding proposes some possibilities of nonlinear effects on beam propagation such as self-focusing and plasma defocusing due to direct interaction of particle cloud with the laser beam. This effect may make the beam to arrive on the surface in Gaussian deviated spatial profile, consequently, the crater is larger and the shape is not perfectly Gaussian. However, the fact that we observe the formation of smaller crater with a rather circular shape and whose square

radius follows pretty well the predicted dependence for a Gaussian beam profile but with a smaller slope, even at high RR values, seems to suggest that such effects should play a minor role in our experimental conditions [14].

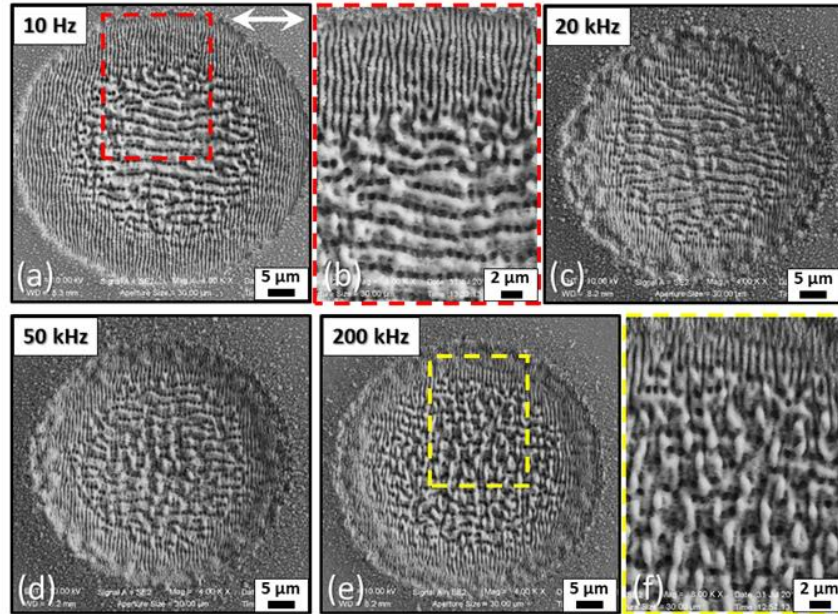


Figure 4.2 SEM images of the irradiated samples at  $N = 200$  pulse and  $E = 10 \mu\text{J}$ , for different values of the pulse repetition rate. Panel (a) shows the image corresponding to 10 Hz that is exemplificative of the crater morphology in the low repetition rate regime. Panel (b) is a zoomed view corresponding to the red box in panel (a). Panels (c), (d) and (e) report SEM images at RR 20, 50 and 200 kHz, respectively. Panel (f) is a zoomed view of the yellow box in panel (e). The arrow in the upper right corner of panel (a) shows the laser beam polarization direction [22].

The SEM images of panels (a) and (b) of Figure 4.2, corresponding to repetition rate  $f_p = 10 \text{ Hz}$ , are representative of the LSFL generated in the low repetition rate regime that consist of sub-wavelength ripples and supra-wavelength grooves oriented along the direction perpendicular and parallel to the laser beam polarization, respectively. The grooves cover a central region with a diameter of  $\approx 32 \mu\text{m}$ , while the ripples are present over an outer annulus with a thickness of  $\approx 10 \mu\text{m}$ . The two structured regions are separated by a very thin transitional area of few microns, as evidenced in the zoomed view of panel (b) in Figure 4.2. Panels (c), (d) and (e) of Figure 4.2 show SEM images registered at  $f_p = 20, 50$  and  $200 \text{ kHz}$ , respectively, illustrating changes occurring at high RR. The SEM images evidence a less regular crater edge and a reduction of the crater

diameter. More interestingly, the LSFL texture of the central part of the crater progressively varies with the pulse RR, while the outer ring of ripples is always present. At  $f_p = 20\text{kHz}$ , in panel (c) of Figure 4.2, the LSFL are rather similar to that observed at lower RR, showing an external rippled area surrounding a central grooved region. At  $f_p = 50\text{ kHz}$ , only few remnants of the grooves observed at lower repetition rates can be recognized, while the texture of the central part varies significantly, eventually displaying a well-developed network of crochet-like structures at  $f_p = 200\text{ kHz}$  (see i.e. panel (f) of Figure 4.2).

Figure 4.3 summarizes the experimental conditions for the formation of the different structures in the central region of the crater, symbolizing the type of surface structures observed for any couple of values of the parameters  $(f_p, F_p)$ . However, as the local value of the fluence degrades from the peak value to the ablation threshold moving towards the periphery, we also consider that ripples are generally formed for values of  $F_p$  from the ablation threshold up to  $F_p \approx 0.3\text{ J/cm}^2$  ( $E = 5.5\text{ }\mu\text{J}$ ), for any value of the repetition rate up to 200 kHz. This is indicated as a reddish-shaded area in Figure 4.3. The other colored areas identify regions of the parameters space in which LSFL can be assigned to grooves (bluish-shaded area) and crochet-like network (yellowish-shaded area), respectively, even if no sharp separation can be precisely defined. Interestingly, for  $F_p \approx 0.35\text{ J/cm}^2$ , we cannot recognize well-formed grooves for  $10\text{ Hz} \leq f_p \leq 1\text{ kHz}$ , while they form in the range  $2\text{ kHz} \leq f_p \leq 20\text{ kHz}$ . At larger values of  $F_p \approx 0.45\text{ J/cm}^2$  and  $\approx 0.5\text{ J/cm}^2$ , grooves are always present unless for the very high RRs, where a crochet-like network is generated. Besides the need for a deeper comprehension of the mechanisms leading to the disappearance of the grooves at the highest values of the parameters  $(f_p, F_p)$  here investigated, the plot of Figure 4.3 displays an interesting playground for the generation of a variety of LSFL by appropriate selection of peak fluence and repetition rate, thus confirming the feasibility of laser surface structuring for the generation of a wide range of surface structures.

We turn now to analyze the profile of the craters obtained by a profilometer and SEM. Figure. 4.4 reports the ablated craters produced by  $N = 100$  laser pulses at an energy  $E = 10\text{ }\mu\text{J}$  and repetition rate of  $f_p = 50\text{ kHz}$ . In this figure, panel (a) shows 3D view of the crater height profile in form of a bi-dimensional false color map. The map shows the formation of a circular crater with a diameter  $D \approx 40\text{ }\mu\text{m}$  (dotted blue circle) surrounded by a rim. As evidenced in the one-

dimensional cross section height profile of Figure 4.3(b), the rim reaches maximum height levels of  $\approx 1 \mu\text{m}$  above the pristine surface of the silicon sample ( $z = 0$ ), while the points of maximum depth in the central area of the crater are located at  $\approx 1 \mu\text{m}$  below the original surface level. Therefore, the generated craters are very shallow as maximum depth and rim heights are  $\approx 40$  times smaller than diameter.

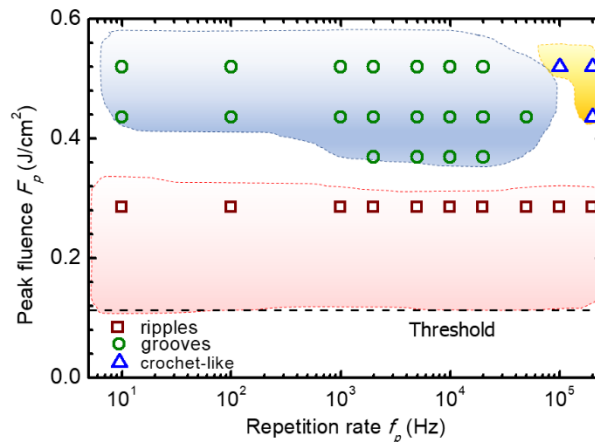


Figure 4.3 Type of LSFL observed for any couple of values of the parameters ( $f_p, F_p$ ). The data refer to irradiation sequences with  $N = 100$  laser pulses. The shaded areas identify regions of the parameters space where the specific LSFL is observed. The reddish-shaded area evidences the region in which ripples are formed considering that they are always present from the edge of the crater corresponding to the ablation fluence threshold up to about  $0.3 \text{ J/cm}^2$ , for all the repetition rates investigated.

The SEM image of the same crater is shown in inset of Figure 4.4 (b). The dashed circles in this SEM image correspond to the three arrows with the same colors in the cross-section profile of Figure 4.4 (b). The green shows the position of the zero-level pristine surface, the blue is the boundary of the crater according to what we see from the SEM and the red displays the location of highest position of rim registered by the profilometer. Considering these three locations on the ablated crater claims that the edges of the spots acquired by the SEM neither match with the zero-level nor the highest position of rim. In fact, it is positioned on a place between the zero-level and the rim; this is possibly due to very much shallow crater and also it depends on the focusing and image contrast of the SEM [22].

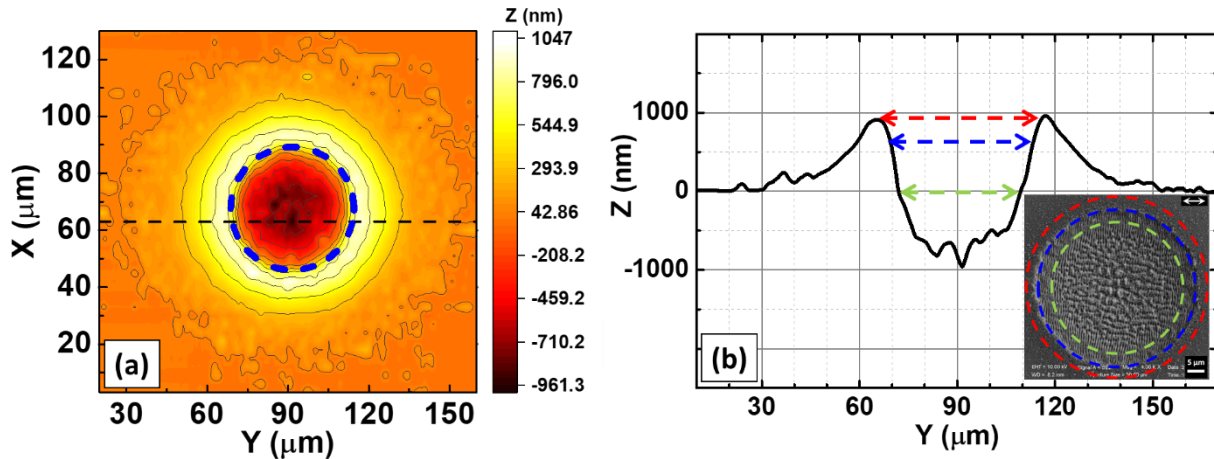


Figure 4.4 Panel (a) displays an example of a profilometer map of the shallow crater produced by a sequence of  $N = 100$  pulses with an energy  $E = 10 \mu\text{J}$  at a pulse repetition rate  $f_p = 50 \text{ kHz}$ . Panel (b) shows a crater cross section profile along the horizontal dashed line reported on the map of panel (a) and crossing the deepest region of the crater. The three double-headed arrows in panel (b) identify the locations of the highest position of the rim (red), of the edge of crater observed by SEM imaging (inset in panel (b)) (blue) and of the locus of the points at height  $z = 0$  corresponding to the original level of the pristine surface of the silicon sample (green), respectively. The dashed circle in panel (a) corresponds to the blue double-headed arrow of panel (b).

Figure 4.5 reports the dependence of crater topographic features on the RR. Figure 4.5 (a) shows the variation of the crater volume and average depth considering the regions below the zero-level pristine level (see the 3D view of the crater registered by profilometry in inset of Figure 4.5 (a)) as a function of pulse repetition rate. The dependence of both parameters on  $f_p$  is consistent with the presence of two different regimes with a sharp transition around 20 kHz. This reduction evidently is happening simultaneously with the sharp reduction of crater size at the same repetition rate, 20 kHz, as it was discussed in Figure 4.1. The same transition is observed for the volume of rim of crater (see Figure 4.5 (b)), where the redeposited ablated particles above the zero-level are located (see inset of Figure 4.5 (b)), as a function of  $f_p$ .

This fact suggests that for the low repetition rate regime ( $f_p < 20 \text{ kHz}$ ), the small variation is related to the intrinsic fluctuations of the ablation process occurring in the typical experimental conditions used in laser surface structuring. Then, a transition occurs to a high pulse repetition rate regime ( $f_p > 20 \text{ kHz}$ ) characterized by a progressive reduction of the ablation efficiency. These results confirm the previous explanation of a progressive reduction of the ablation rate as the RR reaches the tens of kHz region [14].

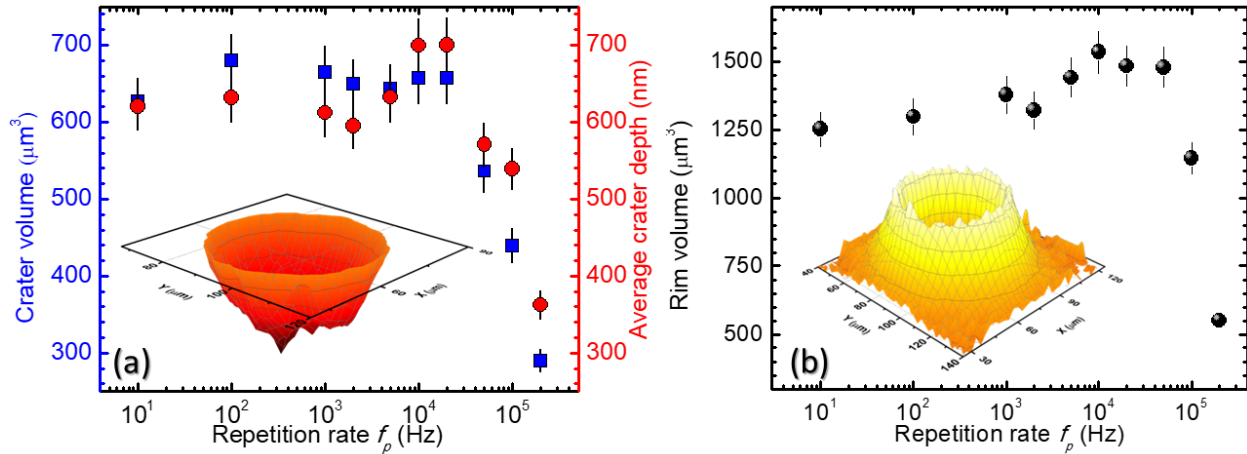


Figure 4.5 Panel (a) reports the variation of the crater volume (circles, left axis) and average crater depth (squares, right axis) on the pulse repetition rate  $f_p$ . Panel (b) shows the dependence of the rim volume as a function the pulse repetition rate  $f_p$ . The data refer to irradiation sequences with  $N = 100$  laser pulses at a pulse energy  $E = 10 \mu\text{J}$ .

To conclude, in this section the generation of quasi-periodic surface features on crystalline silicon irradiated by fs laser pulses was investigated experimentally evidencing a variation in the surface morphology with respect to the RR in the range 10 Hz – 200 kHz. It is found that above-wavelength grooves formation is completely hindered as RR reaches 20 kHz, instead another quasi-periodic feature aligned normal to the polarization is identified. Our experimental results evidence a clear dependence of surface features formation when the same number of laser pulses is delivered to the target but at different repetition rate, in static conditions.

### 4.3 Effect of laser beam wavelength

Most of the experimental investigations on supra-wavelength periodic structures (e.g. grooves) exploit near-infrared Ti:Sa laser sources [5], usually with wavelength  $\lambda \approx 800 \text{ nm}$ , and the spatial period of the grooves typically observed is larger than one micron ( $\Lambda > 1 \mu\text{m}$ ). JJ Nivas et al. observed that the spatial period of the grooves produced by 400 nm fs laser beam shows a value of the order of two times the laser wavelength ( $\Lambda_{groove} \approx 2\lambda_{laser}$ ) [23]. In this section, the results of an experiment carried out at two laser wavelengths to highlight the role of such parameter on the grooves features is reported.

Two set of experiments were carried out using both the fundamental ( $\lambda_{1026} = 1026$  nm) and the second harmonic ( $\lambda_{513} = 513$  nm), generated by a BBO crystal, provided by a Yb:KGW laser system with a pulse duration of  $\approx 180$  fs and a maximum energy of  $\approx 1.5$  mJ. The silicon target was exposed to the laser beam focused using a lens with focal length of 200 mm, in air, at a pulse repetition rate of 1 kHz. The sample was positioned on a XY translation stage. For both wavelengths, LIPSSs were generated in static and dynamic conditions. The laser beam with a Gaussian spatial profile hit the sample at normal incidence. The spot diameter  $D$  at  $1/e^2$  of the maximum laser pulse fluence,  $F_p$  (for pulse energy  $E$ ,  $F_p = 8E/\pi D^2$ ), were estimated to be  $D_{1026} \approx 72$   $\mu\text{m}$  and  $D_{513} \approx 78$   $\mu\text{m}$ .

#### 4.3.1 Grooves formation at both wavelengths $\lambda_{513}$ and $\lambda_{1026}$

A general proposal for explaining the formation mechanism of LSFL for fs irradiation on metal and semiconductors takes into account the absorption of laser pulse energies by electrons. Electron-photon coupling lead this energy to be transferred to the lattice within few picoseconds [6,24]. Considering the fs laser ablation of silicon in different laser wavelengths, the energy absorption in visible regime is higher than that of NIR due to higher level of energy of photons at such wavelengths [23]. This suggests that, at the same laser fluence, irradiation with shorter wavelength gives higher chance of producing grooves [25].

Prior to the experiments in static and dynamic conditions, a set of single craters was realized with various number of pulses  $N$  and laser fluences  $F_p$  in order to evaluate the values of the threshold fluence for grooves formation at the two different wavelengths. The ripple and groove formation threshold fluences  $F_{th}$  were estimated by measuring the laser energy dependence of the radii of grooves and ripples edges from SEM micrographs of the irradiated spots [5]. The determined dependence of  $F_{th}$  of ripples and grooves for  $\lambda_{513}$  and  $\lambda_{1026}$  as a function of number of pulses  $N$  is reported in Figure 4.6 and follows the relation [26]:

$$F_{th}(N) = F_{th}(1) N^{\xi-1} \quad (1)$$

where  $\xi$  is the incubation factor and  $F_{th}(1)$  is the fluence threshold for  $N = 1$ . In Figure 4.6, the solid lines are the fitting curves to the data points. The estimated values of fluence threshold and incubation factors are summarized in the Table 4-1.

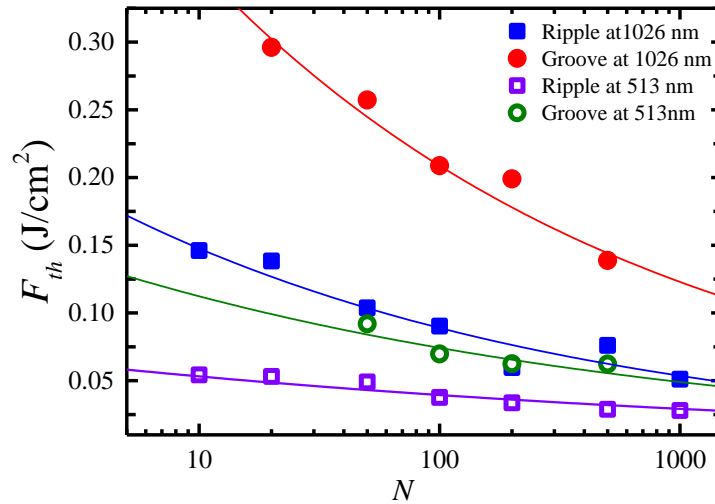


Figure 4.6 Variation of the fluence threshold  $F_{th}$  with the number of pulses  $N$  for ripples and grooves at both wavelengths  $\lambda_{1026}$  and  $\lambda_{513}$ . The uncertainties on the experimental data points are contained within their respective size. The solid lines are a fit to the dependence of Equation (1). The values of the fitting parameters are listed in Table 4-1.

The threshold fluence values and incubation factors are comparable with those reported in the literature [23,26,27]. We observe that the fluence threshold  $F_{th}(1)$  at 513 nm is about 3.5 times lower than that of 1026 nm, confirming the larger effectiveness of ablation and LIPSS formation at the shorter wavelength. This is likely due to a diverse energy coupling efficiency to the silicon target of laser pulses with different wavelengths and to the consequent different level of excitation reached by the irradiated material [23]. In fact, LIPSS features depend on the absorption of laser pulse energies by electrons. Electron-phonon coupling lead this energy to be transferred to the lattice within few picoseconds [6,24]. Considering the properties of silicon for different light wavelengths, absorption in the visible is higher than NIR, thus suggesting that, at the same laser fluence, irradiation with the shorter wavelength gives higher absorbed energy and consequently more chance of producing grooves [25].

Table 4-1 Peak fluence threshold  $F_{th}(1)$ , in  $J/cm^2$ , for  $N = 1$  pulse and incubation factor  $\xi$  for the two wavelengths used in the experiments, namely 513 nm and 1026 nm. The subscripts R and G refer to ripples and grooves, respectively. The peak fluence threshold for ripples corresponds to that needed to produce the shallow ablation crater.

$\lambda$	$F_{th,R}(1)$	$F_{th,G}(1)$	$\xi_R$	$\xi_G$
513 nm	$0.07 \pm 0.02$	$0.17 \pm 0.03$	$0.87 \pm 0.02$	$0.82 \pm 0.06$
1026 nm	$0.25 \pm 0.03$	$0.61 \pm 0.03$	$0.78 \pm 0.04$	$0.77 \pm 0.03$

### 4.3.2 Static laser irradiation mode

In the static mode the target is irradiated at a fixed position by a sequence of  $N$  pulses, at a selected energy  $E$ , producing a shallow crater decorated with LIPSS. Here, we illustrate the morphological features of LIPSSs produced in the center of the craters and their dependence on number of pulses  $N$  and laser pulse peak fluence  $F_p$ . Moreover, the comparison of the observed trends between the two wavelengths is also considered.

Figure 4.7 (a) reports some examples of SEM images of the central region of the irradiated silicon surface registered at various values of  $N$  in the range 50 to 1000, at a laser pulse fluence  $F_p = 0.4 J/cm^2$ , for both wavelengths. Well-developed grooves are observed at both wavelengths for  $50 \leq N \leq 500$ . However, from the SEM images of Figure 4.7 (a), which display areas of the irradiated surface with a similar extension, one can also observe that at 1026 nm the grooves cover a smaller central area and are always surrounded by the ripples, meanwhile at 513 nm they extend over all the frame as a consequence of the much smaller threshold fluence for their formation at the visible wavelength.

Figure 4.7 (b) shows the variation of the grooves period  $\Lambda_G$  (symbols are experimental data) as a function of  $N$  for both wavelengths at a peak fluence  $F_p = 0.4 J/cm^2$ . As the exact value of  $\Lambda_G$  varies with the specific surface location in the grooved area, an average value of the period was estimated, and the observed variability is indicated as an error bar. The data of Figure 4.7(b) show that, at fixed peak fluence,  $\Lambda_G$  progressively increases with  $N$ . This observation results in good agreement with previous experimental findings [23,27] and theoretical predictions, as indicated by the solid lines [1]. Another interesting aspect is the dependence of the grooves period on the laser

wavelength [28]; in Figure 4.7 (b) we observe that the period of the grooves produced at 513 nm is always smaller than at 1026 nm, for the same number of pulses [25].

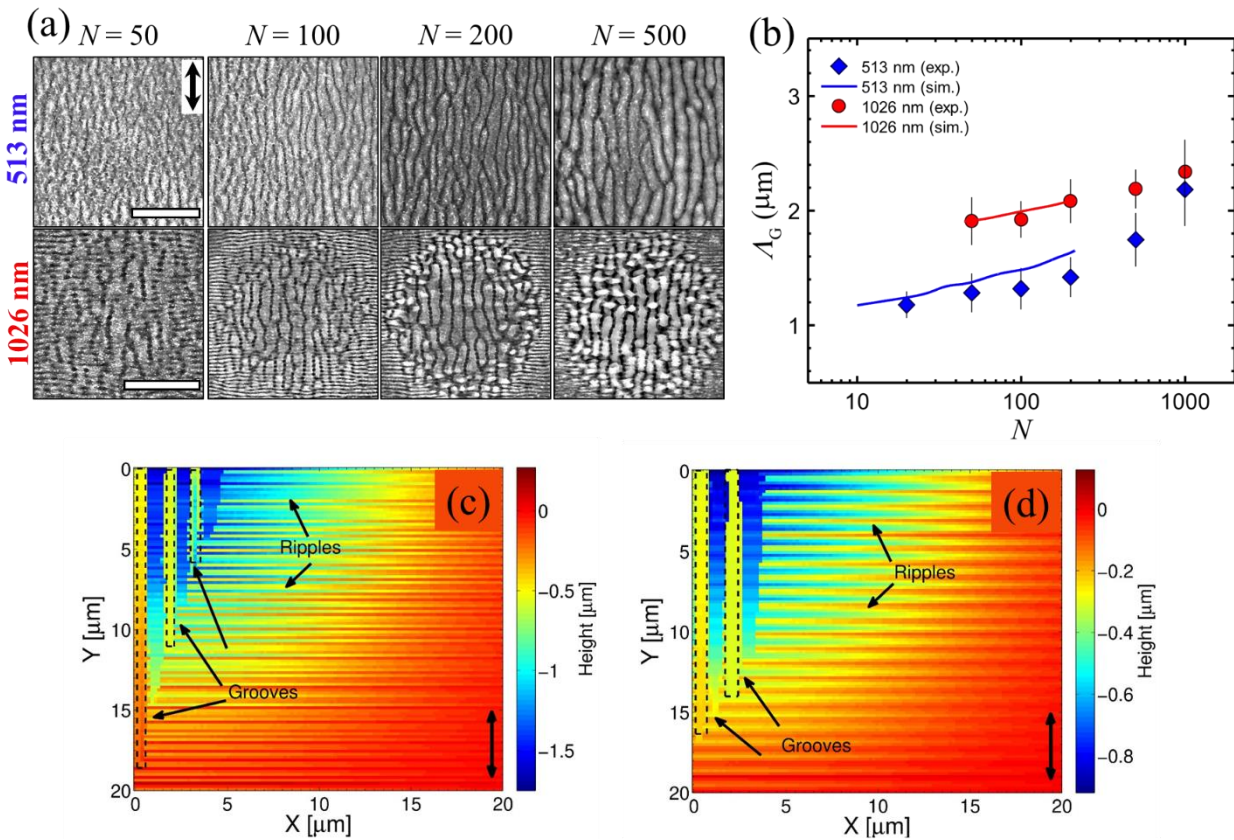


Figure 4.7 Panel (a) reports SEM images of central part of the ablation crater at both  $\lambda_{1026}$  and  $\lambda_{513}$ , for different values of the number of pulses  $N$ . The laser peak fluence  $F_p = 0.4 \text{ J/cm}^2$ . The scale bars shown in the SEM images are 10  $\mu\text{m}$ . the double headed arrow shows the laser beam polarization direction. Panel (b) shows the dependence of the grooves period  $\Lambda_G$  on the number of pulses  $N$  in the range 50÷500, for both  $\lambda_{1026}$  and  $\lambda_{513}$ . The symbols show the experimentally (exp.) and the two solid lines represent the trends predicted by the theoretical simulations (sim.). the simulation results of surface modification for  $F_p \approx 0.4 \text{ J/cm}^2$  for irradiation with  $N = 60$  laser pulses are illustrated at (c) 513 nm and (d) 1026 nm.

Some simulations of the groove's formation process were carried out by George D. Tsibidis (Institute of Electronic Structure and Laser, FORTH) for conditions similar to those used in the experiment. Maps of the silicon target surface after irradiation with peak fluence of  $0.4 \text{ J/cm}^2$  for  $N = 60$  laser pulses for both 513 nm and 1026 nm obtained by the simulations are illustrated in Figure 4.7 (c) and (d). It is evident that ripples are also formed in the periphery of the irradiated area in both cases, but the coverage with grooves is enhanced at the smaller wavelength, in

agreement with the experimental findings of Figure 4.7 (a). Interestingly, the simulations also predict an increasing trend of the grooves period and an approximately similar rate of change on  $N$  as shown by solid lines in Figure 4.7(b). At 513 nm, the simulated values of the grooves period are slightly larger than the experimental one, especially for larger  $N$ , whereas at 1026 nm they are within the experimental error. These differences can be likely due to progressive reduction of the experimental values for damage threshold and LIPSS formation with pulse number  $N$  due to incubation effects [25]. However, the fairly good agreement between the experimental findings and the simulation predictions at the two wavelengths suggest the significance of the underlying hydrothermal waves considered in the model for the generation of grooves.

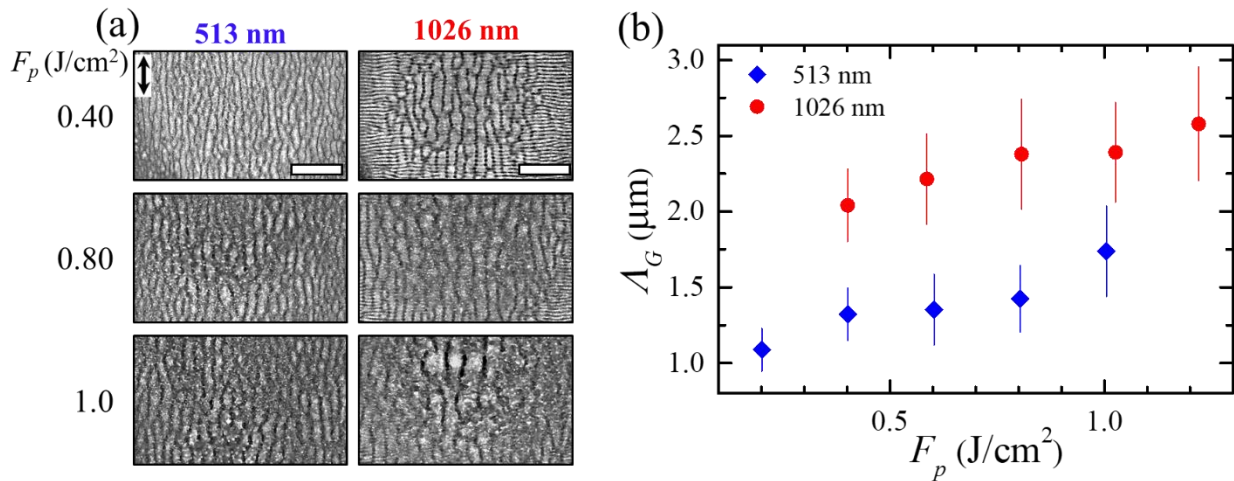


Figure 4.8 Panel (a) reports SEM images exemplifying the variation of the central part of the ablation crater at both  $\lambda_{1026}$  and  $\lambda_{513}$ . for three different values of the peak fluence  $F_p$ , as indicated on the left side of each image. The number of pulses is  $N = 200$ . The scale bars shown in the upper SEM images are  $10 \mu\text{m}$ . The double headed arrow shows the direction of laser beam polarization. Panel (b) shows the variation of the grooves period  $\Lambda_G$  as a function of the peak fluence, for both wavelengths, as measured at  $N = 100$  laser pulses, an experimental condition in which clear grooves are recognized at all the values of the laser fluence shown in the plot.

Figure 4.8 illustrates the variation of the grooves with the laser peak fluence  $F_p$ . Panel (a) of Figure 4.8 reports typical SEM images of the central part of the ablation crater at both  $\lambda_{513}$  and  $\lambda_{1026}$ . Here, for the sake of simplification, only three different values of the peak fluence  $F_p$ , at a pulse number  $N = 200$ , are shown. Panel (b) of Figure 4.8 shows the dependence of the grooves period  $\Lambda_G$  on the peak fluence  $F_p$ , for both wavelengths. The number of pulses  $N = 100$  is considered here since it allows displaying more data points for the wavelength  $\lambda_{1026}$ , but a similar trend occurs

at  $N = 200$  as well. At both wavelengths,  $A_G$  increases linearly with the laser peak fluence  $F_p$  [25], which seems in agreement with recent theoretical and experimental results on steel [6] but that deserve still theoretical confirmation for the case of silicon.

### 4.3.3 Scanning laser irradiation mode

The experimental performance for laser irradiation in dynamic mode aims at investigating the possibility of producing grooves by moving the silicon sample at different scan velocities. This achievement is important due to the industrial demands for large area laser processing.

Figure 4.9 shows the SEM images of the silicon surfaces under dynamic laser irradiation mode for both wavelengths. The fabrication of scanned lines was done using the same laser system of the static irradiation mode at a pulse repetition rate  $f_p = 1$  kHz and a peak fluence  $F_p = 0.4$  J/cm<sup>2</sup>. Four different values of the scan speed  $v_s$ , namely  $v_s = 1, 0.5, 0.25, 0.1$  mm/s, are selected. Due to the slight difference in the values of the laser spot diameter  $D$  for the two wavelengths, the number of overlapped pulses  $N_o = D f_p / v_s$  have slightly different values, namely {78, 156, 312, 780} at 513 nm and {72, 144, 288, 720} at 1026 nm, corresponding to the scan speeds of {1, 0.5, 0.25, 0.1}, respectively.

Presence of supra-wavelength grooves, oriented parallel to the direction of laser polarization, is evident under irradiation with 513 nm for all four values of the scan speed (upper panels of Figure 4.9). From the SEM images we can observe a qualitative trend of increasing spatial period as the surface scan gets slower and the number of overlapped pulses increases. On the other hand, the scanned lines at 1026 nm (lower panels of Figure 4.9) display formation of well-developed grooves in conditions of higher overlapped pulse and lower scan speeds. In particular, presence of grooves at a scan speed of 1 mm/s (Figure 4.9 (a)) is not clearly recognizable as much as ripples. Moreover, slower scans result in thicker grooves (i.e. Figure 4.9 (h)). These observations are coherent with the variation of the surface structures on the pulse number  $N$  observed in static irradiation conditions in section 4.3.2.

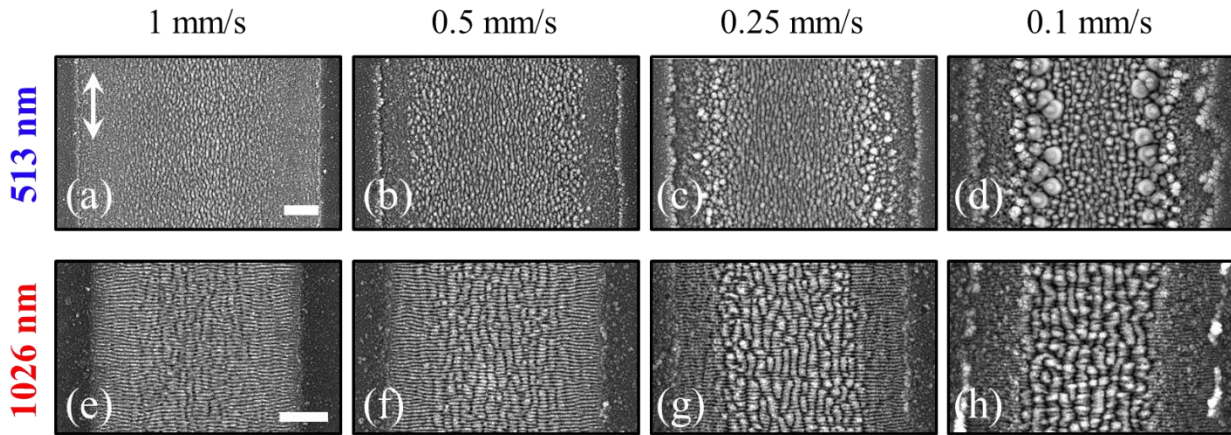


Figure 4.9 SEM images of the silicon surfaces after irradiation with laser peak fluence  $F_p \approx 0.4 \text{ J/cm}^2$  and repetition rate  $f_p = 1 \text{ kHz}$  for four values of the scan speed  $v_s$  (e.g.  $v_s = 1, 0.5, 0.25, 0.1 \text{ mm/s}$ ), as indicated above each column. Panels (a-d) correspond to surface structuring with 513 nm, while panels (e-h) with 1026 nm, respectively. The number of overlapped pulses,  $N_O$  is: (a) 78; (b) 156; (c) 312; (d) 780; (e) 72; (f) 144; (g) 288; (h) 720. The scale bar is equal to  $10 \mu\text{m}$ . The double-headed arrow in panel (a) shows the laser polarization direction for all panels.

Figure 4.10 reports a direct morphological comparison of fine structures formed in the central region of craters between static and scanning laser irradiation with laser peak fluence of  $F_p = 0.4 \text{ J/cm}^2$  for each laser wavelengths. The upper images in both panels (Fig. 4.10 (a) and (b)) display SEM images of the craters in static condition after irradiation with a sequence of  $N = 200$  laser pulses for 513 nm and 1026 nm. While, the lower SEM images show the lines obtained with scan speed of  $0.25 \text{ mm/s}$  at 513 nm and 1026 nm. For all cases, zoomed views are shown on the sides in dashed boxes. These images confirm that the general characteristics of the irradiated surface are rather similar in the two experimental conditions. In fact, in both modes of irradiation, at 513 nm (see Figure 4.10 (a)) a central grooved region is surrounded by the region covered with rudiment of grooves, while at 1026 nm (see Figure 4.10 (b)) grooves and ripples cover the central and outer regions, respectively. The similarities of morphologies in static and dynamic conditions suggest that a similar formation mechanism for grooves generation: the energy redistribution induced by the electromagnetic mechanisms is related to the generation of surface scattered waves induced by the sample roughness and by the already formed ripples [4,5].

However, the zoomed views of Figure 4.10 show some differences in the finer morphological features of the structures. In particular, the grooves show a larger granularity in the scanning regime at 513 nm and a more evident underlying layer of ripples at 1026 nm. These characteristics

can be likely associated to the fact that while with static irradiation each point of the surface receives the same amount of laser fluence in each shot, in scanning mode the local value of the fluence varies continuously with the laser shot (or time) [25].

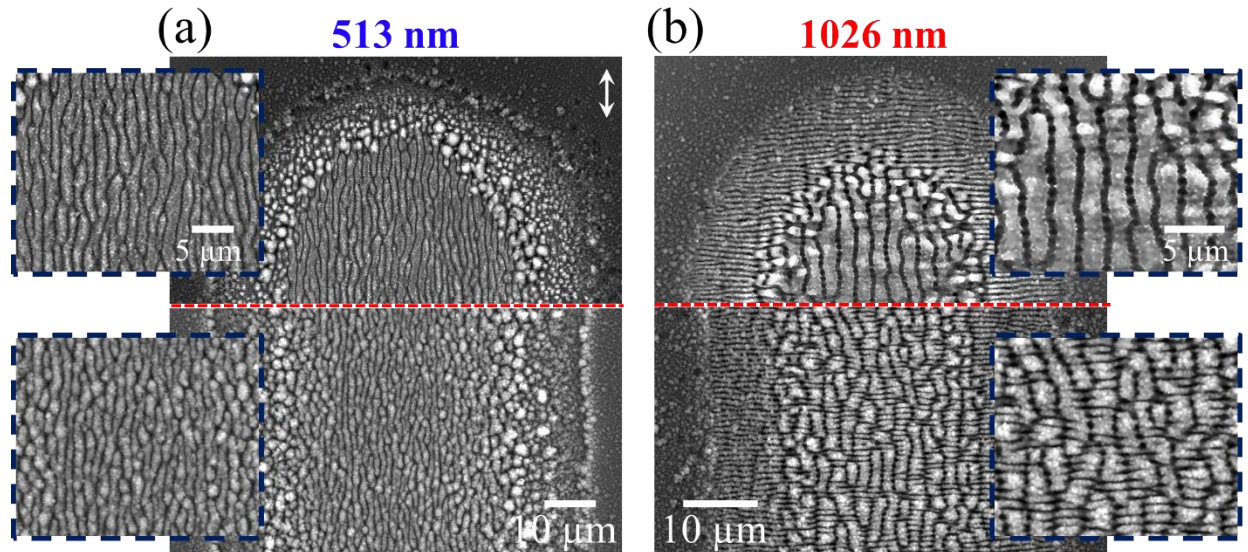


Figure 4.10 Comparison of the surface structures for static and dynamic irradiation conditions at the two wavelengths: (a) 513 nm; (b) 1026 nm. In both cases the laser peak fluence is  $F_p = 0.4 \text{ J/cm}^2$ . The upper SEM images refer to static irradiation conditions with a number of pulses  $N = 200$ . The lower SEM images refer to dynamic irradiation conditions for a scan speed  $v_s$  of 0.25 mm/s, corresponding to a number of overlapped pulses  $N_o$  of 312 at 513 nm and 288 at 1026 nm. The images in dashed boxes next to each image shows the zoomed views. The scale bar in full views are 10  $\mu\text{m}$  and in zoomed views 5  $\mu\text{m}$ . The double headed arrow in panel (a) shows the laser polarization direction.

#### 4.4 Effect of ambient pressure on formation of grooves

In previous sections, we have seen that the irradiation conditions play a crucial role on the formation of LIPSSs; however, mechanisms of surface structures formation are still debated. Zayats et al. reported that scattering of surface plasmon polaritons (SPPs) can result from surface roughness [29]. Therefore, the next laser pulses combine with the SPPs of previous produced nanostructures which causes a periodic spatial modulation of energy onto the surface irradiated by a linearly polarized laser beam [3,30]. The surrounding media is another parameter influencing the morphological features of LIPSS. Apart from air which is the most common ambient in which the surface structures are produced, already discussed in previous sections, several studies considered the case of liquid environment [31–33], but very few investigated the development of LIPSS in

high vacuum or at variable ambient air pressure. JJ Nivas et al. [34] performed studies on the formation of LIPSS in high vacuum condition ( $\approx 10^{-5}$  mbar) in order to minimize the presence of redeposited nanoparticles on the ablated crater. They have reported the comparison of morphological features of LIPSS in atmospheric and vacuum pressures [34–36].

In this section, the effect of variation of the ambient air pressure on the spatial period of ripples, formation of grooves and shape of the craters is analyzed. Moreover, the effects of various states of polarization in vacuum as well as of circularly polarized pulses in air vs vacuum are also addressed. In these experiments the silicon target is positioned on a XY-translation stage inside a vacuum chamber and irradiated using a Nd: Glass laser system delivering linearly polarized  $\approx 900$  fs pulses at 1055 nm at a repetition rate of 33 Hz, with a Gaussian spatial profile. An electromechanical shutter provides the selection of the desired number of laser pulses,  $N$ , applied to the same spot on the target. Experiments are carried out in the residual air pressure going from atmospheric pressure to high vacuum, at a base pressure of  $\approx 10^{-4}$  mbar. The beam focal spot radius on the target is determined by measuring the energy variation of the ablation crater dimensions [37], resulting in  $w_0 = (130 \pm 5) \mu\text{m}$ .

#### 4.4.1 Effect of pressure variation

Figure 4.11 reports SEM and AFM images of the ripples on silicon surfaces produced at various pressures  $p$ . The sample was irradiated at a peak fluence of  $\approx 0.3 \text{ J/cm}^2$ .

Figure 4.11 (a) and (b) are exemplificative images of ripples produced in different pressure conditions for  $N = 100$ . They address a variation of the spatial period  $\Lambda$  and depth  $\delta$  of ripples with the pressure  $p$ . The data are summarized in table 4-2.  $\delta$  was estimated by evaluating the maximum peak-to-valley height (by using the image processing software Gwyddion). The measured data show a strong dependence of the ripples' period  $\Lambda$  on  $p$  with a reduction of  $\Lambda$  and a corresponding increase of  $\delta$  as  $p$  raises to higher values. Moreover, the ripples generated in vacuum present a larger average period, a wider characteristic thickness, and a narrower separation with respect to air [38].

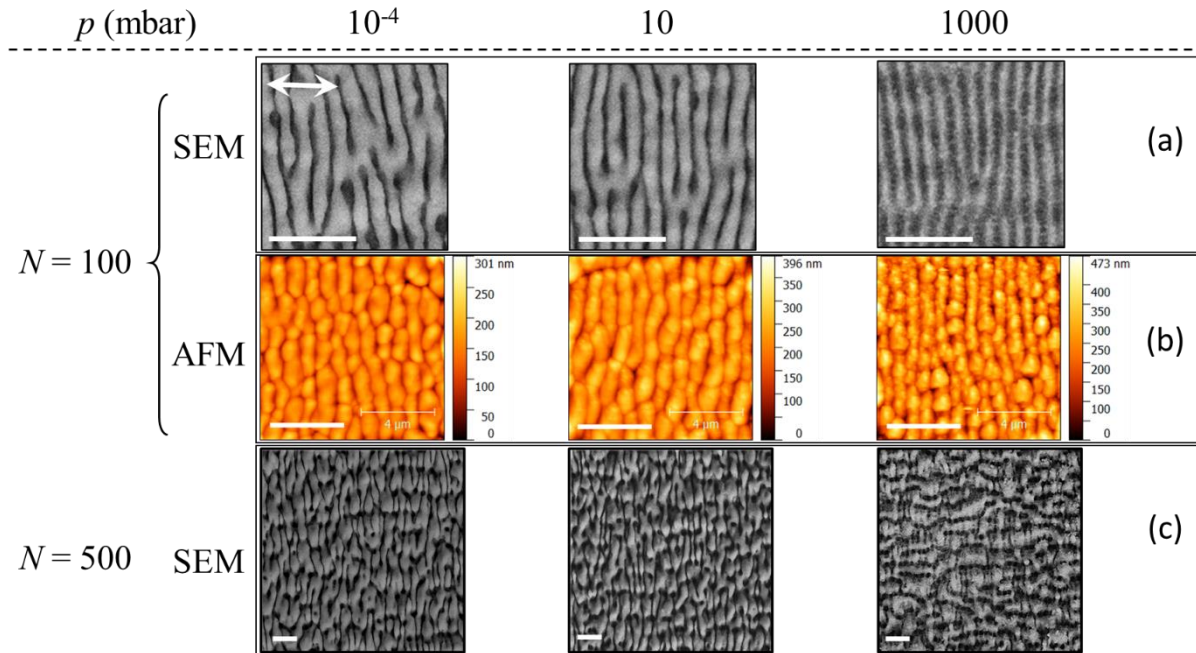


Figure 4.11 Examples of SEM and AFM images for a peak fluence of  $\approx 0.3 \text{ J/cm}^2$  and various values of the pressure  $p$  of (a) and (b) the ripples generated by irradiation with  $N = 100$  laser pulses and (c) the central region of the targets irradiated with  $N = 500$  laser pulses. The scale bar in each panel is  $4 \mu\text{m}$ . The double-headed arrow in the upper left panel shows the direction of the laser polarization

Panel (c) of Figure 4.11 illustrates the SEM images of the central region of the crater at  $N = 500$  pulses and for various pressure conditions. At atmospheric pressure,  $p = 1000 \text{ mbar}$ , the typical grooves with a preferential orientation parallel to the laser polarization are observed. However, at the lower pressures of  $10 \text{ mbar}$  and  $10^{-4} \text{ mbar}$  the central region of the irradiated spot presents rather different morphological features with respect to the grooves observed at atmospheric pressure.

Table 4-2 Values of the ripples period  $\Lambda$  obtained by SEM and AFM analyses and depth  $\delta$  measured by AFM. As the values of the measured parameters varies with spatial location, the data are given as estimated mean value and standard deviation.

$p$ (mbar)	SEM	AFM	
	$\Lambda$ (nm)	$\Lambda$ (nm)	$\delta$ (nm)
$10^{-4}$	$918 \pm 58$	$964 \pm 69$	$91 \pm 4$
10	$866 \pm 45$	$933 \pm 40$	$139 \pm 7$
1000	$785 \pm 38$	$796 \pm 46$	$216 \pm 12$

In high vacuum conditions, the surface texture shows a kind of multicellular patterns formed by elemental components with a length varying in the range of few to tens of  $\mu\text{m}$  and showing a preferential elongation in the direction normal to the laser polarization. This suggests that their formation should result from a merging of two or more adjacent ripples induced by the higher value of the fluence in the central region of the laser beam spot and the iterated irradiation. The fact that grooves do not form at reduced pressure suggests a possible important role of nanoparticles in the formation of these supra-wavelength surface structures. In fact, at atmospheric pressure the ablated nanoparticles get re-deposited on the sample surface and influence the formation of surface structures. As the pressure is lower, the ablated material is less confined with a reduction of re-deposition of ablated particles that more easily fly away from the target surface [38,39]. As for the ripples under high vacuum pressure, the anti-correlation between period and depth of ripples results from slightly changes in effective refractive index of the surface due to different modification of nanoparticles. This effect is shown in Figure 4.12: in air, a rim of aggregated nanoparticles is visible around the structured area (Figure 4.12 (c) and its zoomed view in Figure 4.12 (d)); in vacuum, such an effect seems almost negligible (Figure 4.12 (a) zoomed view in Figure 4.12 (b)) The disappearance of the grooves at lower pressure and the simultaneous sizeable reduction of the nanoparticles seem in fairly good agreement with Sipe–Drude theory for a rough surface, further addressing the nanoparticulate as a key factor for grooves generation, besides any possible other hydrodynamic mechanism [40,41] or the possible influence of ambient oxygen.

Figures 4.12 (a) and (c) highlight the variation of size and crater shape from circle to elliptic as the pressure goes down from vacuum to air. In vacuum,  $p = 10^{-4}$  mbar, the spot turns to more oval shape along the direction of laser beam polarization. The plot in Figure 4.12 (e) which is the ratio between minor and major diameter vs pressure  $p$ , clarifies that craters at lower number of pulses  $N$  and pressure  $p$  are more elliptic. The different size can likely result from an enhanced absorption associated with the rougher developing surface in air. In fact, the dense coverage with nanoparticles and nanostructures generated by multi-pulse fs laser irradiation progressively modifies the surface absorption properties [39].

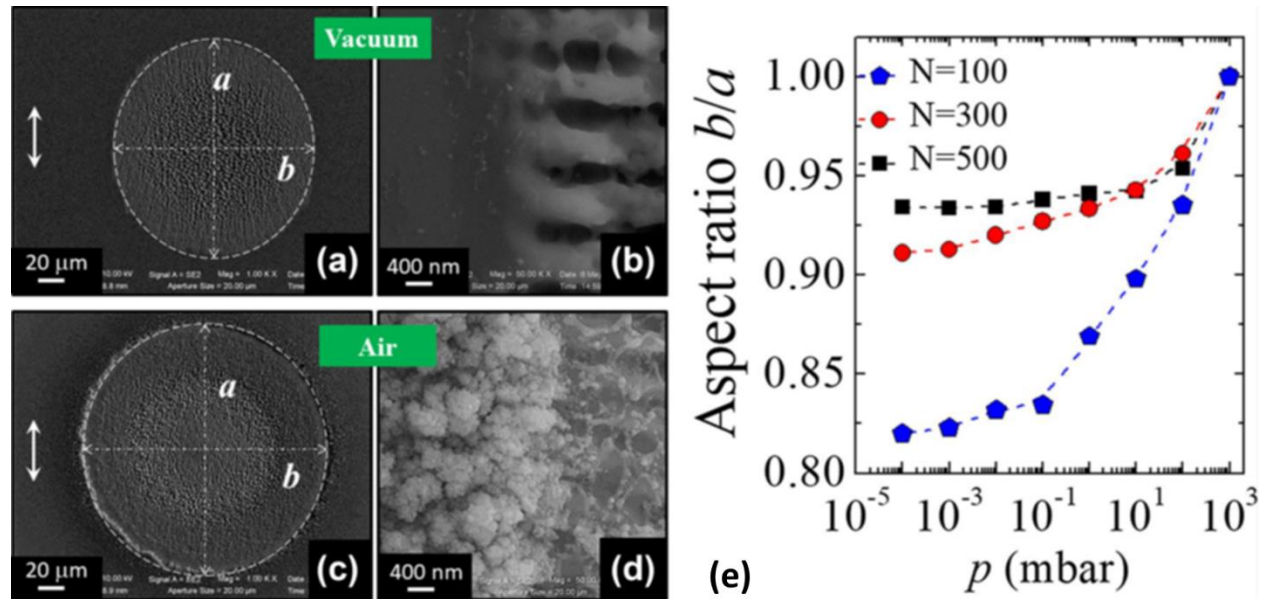


Figure 4.12 Panels (a) and (c) report SEM images of the surface structured area ( $N = 300$  laser pulses, peak fluence  $\approx 0.3 \text{ J/cm}^2$ ) in vacuum ( $p \approx 10^{-4} \text{ mbar}$ ) and air illustrating the effect of the pressure on its shape and size. Panels (b) and (d) are zoomed views evidencing the different nanoparticles coverage at the edge of the structured area in the two cases. Panel (e) reports the variation of the aspect ratio  $b/a$  as a function of the pressure for various number of pulses  $N$ . The double headed arrow in the panels (a) and (b) shows the direction of the laser polarization.

#### 4.4.2 Effect of the laser polarization under vacuum condition

Further investigations on the effect of the state of laser polarization on the shape of crater and features of the fine structures have been done. Figure 4.13 reports the SEM images of ablated craters comparing four different states of polarization of the laser beam produced by means of waveplates (half or quarter for linear and circular polarization, respectively) in low pressure of  $10^{-4} \text{ mbar}$ . Vertical and horizontal linear polarizations result in elliptical craters with the major axes following the laser beam polarization (panels (a) and (b) of Figure 4.13). The zoomed views of panels (a) and (b), in dashed yellow boxes on their sides, display the presence of ripples on the edges of the craters. In case of vertical laser polarization (panel (b)), it is evident that the formation of ripples ends abruptly, and this side of the crater is parallel to the polarization. On the other hand, in panel (a), the rippled regions protruding outwards along the polarization direction can be due to generation of surface-scattered electromagnetic waves (SSW) favoured by ripples grating and surface roughness. The interference of the SSW with the low-energy tail of the laser beam can favor the formation of the rippled protrusions also in peripheral areas in which the laser beam alone

would not exceed the threshold fluence for the creation of surface structures at that number of pulses. This, in turn, should explain the development of the elliptically shaped spot with major axis directed along the laser polarization, as observed experimentally [35,39].

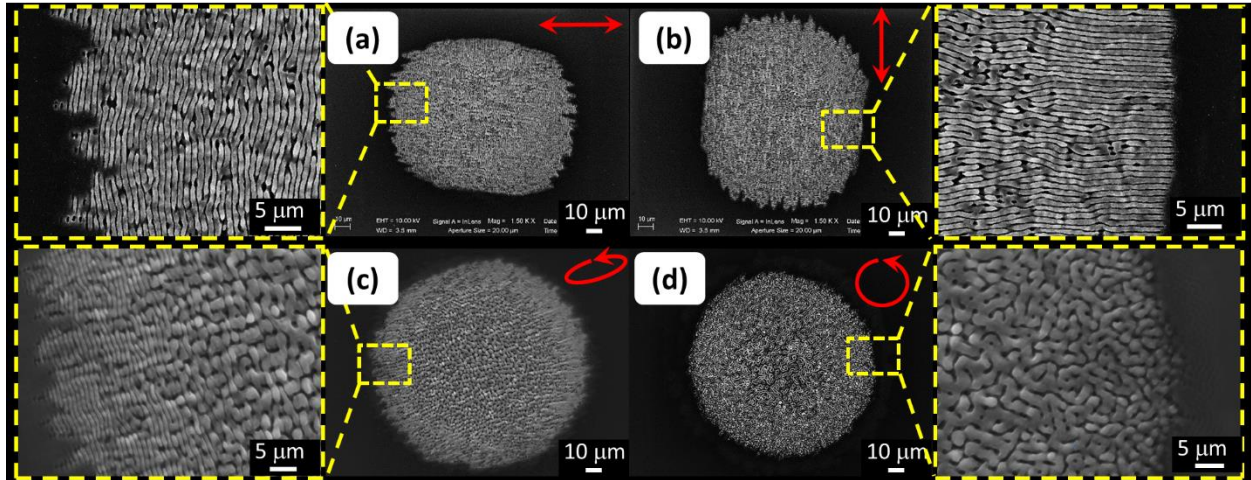


Figure 4.13 SEM images of the surface structures produced in vacuum ( $p \sim 10^{-4}$  mbar) with various state of polarizations. Panels (a) and (b) show images of the spot produced with (a) horizontal and (b) vertical linear polarization ( $N = 200$  pulse at a fluence of  $\approx 0.25$  J/cm<sup>2</sup>). Panels (c) and (d) report images of the spot produced with (c) elliptical and (d) circular polarizations ( $N = 300$  pulse at a fluence of  $\approx 0.3$  J/cm<sup>2</sup>), respectively. The images in the yellow dashed boxes show zoomed views of the spot edge illustrating the surface structures formed by the different states of polarization.

Elliptical polarization (Figure 4.13 (c)) results in a nearly-circular spot only slightly longer in the direction of the prevailing axis of the polarization ellipse. Moreover, ripples directed along the normal to the prevailing linear component of the elliptically polarized beam are formed at the periphery of the spot. Instead, the circular polarization (Figure 4.13 (d)) produces an almost circular spot with a texture resembling a tangle of randomly oriented elements. Moreover, the central region of the spots is characterized by a pattern composed of coarser elemental constituents with respect to those present at the edges. This can likely result from thermal fusion processes (coalescence) of two or more elemental structures in the region of higher laser fluence.

The outputs of the above-mentioned experiments suggest a crucial role of the ambient pressure on the development of surface structures. The results highlight that as the pressure raises the ablated nanoparticles produced during the fs laser ablation process of the target get deposited more and

more on the sample surface covering the irradiated spot area and influencing the structuring process and possibly the formation of grooves.

## References

- [1] G.D. Tsibidis, C. Fotakis, E. Stratakis, From ripples to spikes: A hydrodynamical mechanism to interpret femtosecond laser-induced self-assembled structures, *Phys Rev B - Condens Matter Mater Phys.* 92 (2015) 1–6. <https://doi.org/10.1103/PhysRevB.92.041405>.
- [2] J. Bonse, S. Hohm, S. V. Kirner, A. Rosenfeld, J. Kruger, Laser-Induced Periodic Surface Structures-A Scientific Evergreen, *IEEE J Sel Top Quantum Electron.* 23 (2017). <https://doi.org/10.1109/JSTQE.2016.2614183>.
- [3] A.Y. Vorobyev, C. Guo, Direct femtosecond laser surface nano/microstructuring and its applications, *Laser Photon Rev.* 7 (2012) 385–407. <https://doi.org/10.1002/lpor.201200017>.
- [4] S. He, J.J. Nivas, K.K. Anoop, A. Vecchione, M. Hu, R. Bruzzese, S. Amoroso, Surface structures induced by ultrashort laser pulses: Formation mechanisms of ripples and grooves, *Appl Surf Sci.* 353 (2015) 1214–1222. <https://doi.org/10.1016/j.apsusc.2015.07.016>.
- [5] S. He, J. JJ Nivas, A. Vecchione, M. Hu, S. Amoroso, On the generation of grooves on crystalline silicon irradiated by femtosecond laser pulses, *Opt Express.* 24 (2016) 3238–3247. <https://doi.org/10.1364/OE.24.003238>.
- [6] G.D. Tsibidis, A. Mimidis, E. Skoulas, S. V. Kirner, J. Krüger, J. Bonse, E. Stratakis, Modelling periodic structure formation on 100Cr6 steel after irradiation with femtosecond-pulsed laser beams, *Appl Phys A Mater Sci Process.* 124 (2018). <https://doi.org/10.1007/s00339-017-1443-y>.
- [7] R. Le Harzic, D. Dörr, D. Sauer, M. Neumeier, M. Epple, H. Zimmermann, F. Stracke, Large-area, uniform, high-spatial-frequency ripples generated on silicon using a nanojoule-femtosecond laser at high repetition rate, *Opt Lett.* 36 (2011) 229. <https://doi.org/10.1364/ol.36.000229>.
- [8] A. Gruner, J. Schille, U. Loeschner, Experimental study on micro hole drilling using ultrashort pulse laser radiation, *Phys Procedia.* 83 (2016) 157–166. <https://doi.org/10.1016/j.phpro.2016.08.030>.
- [9] G. Kamlage, T. Bauer, A. Ostendorf, B.N. Chichkov, Deep drilling of metals by femtosecond laser pulses, *Appl Phys A Mater Sci Process.* 77 (2003) 307–310. <https://doi.org/10.1117/12.482108>.
- [10] X. Sedao, M. Lenci, A. Rudenko, A. Pascale-Hamri, J.P. Colombier, C. Mauclair, Additive and subtractive surface structuring by femtosecond laser induced material ejection and redistribution, *Materials (Basel).* 11 (2018) 2456. <https://doi.org/10.3390/ma11122456>.

- [11] R. Weber, T. Graf, P. Berger, V. Onuseit, M. Wiedenmann, C. Freitag, A. Feuer, Heat accumulation during pulsed laser materials processing: erratum, *Opt Express*. 22 (2014). <https://doi.org/10.1364/OE.22.011312>.
- [12] X. Sedao, M. Lenci, A. Rudenko, N. Faure, A. Pascale-Hamri, J.P. Colombier, C. Mauclair, Influence of pulse repetition rate on morphology and material removal rate of ultrafast laser ablated metallic surfaces, *Opt Lasers Eng.* 116 (2019) 68–74. <https://doi.org/10.1016/j.optlaseng.2018.12.009>.
- [13] G. Raciukaitis, M. Brikas, P. Gecys, M. Gedvilas, Accumulation effects in laser ablation of metals with high-repetition-rate lasers, *SPIE Proceedings, High-Power Laser Ablation VII*. 7005 (2008) 70052L. <https://doi.org/10.1117/12.782937>.
- [14] E. Allahyari, J.J.J. Nivas, M. Valadan, R. Fittipaldi, A. Vecchione, L. Parlato, R. Bruzzese, C. Altucci, S. Amoruso, Plume shielding effects in ultrafast laser surface texturing of silicon at high repetition rate in air, *Appl Surf Sci.* 488 (2019) 128–133. <https://doi.org/10.1016/j.apsusc.2019.05.219>.
- [15] A. Ancona, K. Rademaker, F. Röser, J. Limpert, S. Nolte, A. Tünnermann, Laser drilling using a high repetition rate and high average power femtosecond fiber CPA system, *Opt InfoBase Conf Pap.* 16 (2008) 593–596. <https://doi.org/10.1109/CLEO.2008.4551313>.
- [16] S.M. Eaton, H. Zhang, P.R. Herman, F. Yoshino, L. Shah, J. Bovatsek, A.Y. Arai, Heat accumulation effects in femtosecond laser-written waveguides with variable repetition rate, *Opt Express*. 13 (2005) 4708. <https://doi.org/10.1364/opex.13.004708>.
- [17] I. Gnilitzkyi, V. Gruzdev, N.M. Bulgakova, T. Mocek, L. Orazi, Mechanisms of high-regularity periodic structuring of silicon surface by sub-MHz repetition rate ultrashort laser pulses, *Appl Phys Lett.* 109 (2016) 143101. <https://doi.org/10.1063/1.4963784>.
- [18] M.E. Povarnitsyn, T.E. Itina, M. Sentis, K. V. Khishchenko, P.R. Levashov, Material decomposition mechanisms in femtosecond laser interactions with metals, *Phys Rev B.* 75 (2007) 235414. <https://doi.org/10.1103/PhysRevB.75.235414>.
- [19] P. Lorazo, L.J. Lewis, M. Meunier, Thermodynamic pathways to melting, ablation, and solidification in absorbing solids under pulsed laser irradiation, *Phys Rev B.* 73 (2006) 134108. <https://doi.org/10.1103/PhysRevB.73.134108>.
- [20] S. Amoruso, R. Bruzzese, N. Spinelli, R. Velotta, M. Vitiello, X. Wang, G. Ausanio, V. Iannotti, L. Lanotte, Generation of silicon nanoparticles via femtosecond laser ablation in vacuum, *Appl Phys Lett.* 84 (2004) 4502–4504. <https://doi.org/10.1063/1.1757014>.
- [21] N. Tsakiris, K.K. Anoop, G. Ausanio, M. Gill-Comeau, R. Bruzzese, S. Amoruso, L.J. Lewis, Ultrashort laser ablation of bulk copper targets: Dynamics and size distribution of the generated nanoparticles, *J Appl Phys.* 115 (2014). <https://doi.org/10.1063/1.4885196>.
- [22] E. Allahyari, J.J. Nivas, G. Avallone, M. Valadan, M. Singh, V. Granata, C. Cirillo, A. Vecchione, R. Bruzzese, C. Altucci, S. Amoruso, Femtosecond laser surface irradiation of

- silicon in air: pulse repetition rate influence on removal efficiency and surface texture, Submitted. (n.d.).
- [23] J.J. Nivas, K.K. Anoop, R. Bruzzese, R. Philip, S. Amoruso, Direct femtosecond laser surface structuring of crystalline silicon at 400 nm, *Appl Phys Lett.* 112 (2018) 121601. <https://doi.org/10.1063/1.5011134>.
- [24] F. Fraggelakis, G. Mincuzzi, J. Lopez, I. Manek-Hönninger, R. Kling, Controlling 2D laser nano structuring over large area with double femtosecond pulses, *Appl Surf Sci.* 470 (2019) 677–686. <https://doi.org/10.1016/j.apsusc.2018.11.106>.
- [25] E. Allahyari, J.J. Nivas, E. Skoulas, R. Bruzzese, G.D. Tsibidis, E. Stratakis, S. Amoruso, On the formation and features of the supra-wavelength grooves generated during femtosecond laser surface structuring of silicon, *Manuscr under Prep to Submit J Appl Surf Sci.* (2020).
- [26] J. Bonse, S. Baudach, J. Krüger, W. Kautek, M. Lenzner, Femtosecond laser ablation of silicon-modification thresholds and morphology, *Appl Phys A.* 74 (2002) 19–25. <https://doi.org/10.1007/s003390100893>.
- [27] J.J.J. Nivas, S. He, A. Rubano, A. Vecchione, D. Paparo, L. Marrucci, R. Bruzzese, S. Amoruso, Direct Femtosecond Laser Surface Structuring with Optical Vortex Beams Generated by a q-plate, *Sci Rep.* 5 (2015) 17929. <https://doi.org/10.1038/srep17929>.
- [28] G.D. Tsibidis, E. Skoulas, A. Papadopoulos, E. Stratakis, Convection roll-driven generation of supra-wavelength periodic surface structures on dielectrics upon irradiation with femtosecond pulsed lasers, *Phys Rev B.* 94 (2016) 081305(R). <https://doi.org/10.1103/PhysRevB.94.081305>.
- [29] A. V. Zayats, I.I. Smolyaninov, Near-field photonics: Surface plasmon polaritons and localized surface plasmons, *J Opt A Pure Appl Opt.* 5 (2003). <https://doi.org/10.1088/1464-4258/5/4/353>.
- [30] A.Y. Vorobyev, V.S. Makin, C. Guo, Periodic ordering of random surface nanostructures induced by femtosecond laser pulses on metals, *J Appl Phys.* 101 (2007). <https://doi.org/10.1063/1.2432288>.
- [31] S. Bashir, M.S. Rafique, C.S. Nathala, A.A. Ajami, W. Husinsky, Femtosecond laser fluence based nanostructuring of W and Mo in ethanol, *Phys B Condens Matter.* 513 (2017) 48–57. <https://doi.org/10.1016/j.physb.2017.03.008>.
- [32] R. Kuladeep, M.H. Dar, K.L.N. Deepak, D.N. Rao, Ultrafast laser induced periodic sub-wavelength aluminum surface structures and nanoparticles in air and liquids, *J Appl Phys.* 116 (2014). <https://doi.org/10.1063/1.4896190>.
- [33] C. Albu, A. Dinescu, M. Filipescu, M. Ulmeanu, M. Zamfirescu, Periodical structures induced by femtosecond laser on metals in air and liquid environments, *Appl Surf Sci.* 278 (2013) 347–351. <https://doi.org/10.1016/j.apsusc.2012.11.075>.

- [34] J.J.J. Nivas, Z. Song, R. Fittipaldi, A. Vecchione, R. Bruzzese, S. Amoruso, Direct ultrashort laser surface structuring of silicon in air and vacuum at 1055 nm, *Appl Surf Sci.* 417 (2017) 149–154. <https://doi.org/10.1016/j.apsusc.2017.03.158>.
- [35] F. Gesuele, J. JJ Nivas, R. Fittipaldi, C. Altucci, R. Bruzzese, P. Maddalena, S. Amoruso, Analysis of nascent silicon phase-change gratings induced by femtosecond laser irradiation in vacuum, *Sci Rep.* 8 (2018) 0–10. <https://doi.org/10.1038/s41598-018-30269-0>.
- [36] F. Gesuele, J.J.J. Nivas, R. Fittipaldi, C. Altucci, R. Bruzzese, P. Maddalena, S. Amoruso, Multi-imaging analysis of nascent surface structures generated during femtosecond laser irradiation of silicon in high vacuum, *Appl Phys A Mater Sci Process.* 124 (2018). <https://doi.org/10.1007/s00339-018-1633-2>.
- [37] J.M. Liu, Simple technique for measurements of pulsed Gaussian-beam spot sizes, *Opt Lett.* 7 (1982) 196. <https://doi.org/10.1364/OL.7.000196>.
- [38] J. JJ Nivas, F. Gesuele, E. Allahyari, S.L. Oscurato, R. Fittipaldi, A. Vecchione, R. Bruzzese, S. Amoruso, Effects of ambient air pressure on surface structures produced by ultrashort laser pulse irradiation, *Opt Lett.* 42 (2017) 2710. <https://doi.org/10.1364/ol.42.002710>.
- [39] J. JJ Nivas, E. Allahyari, F. Gesuele, P. Maddalena, R. Fittipaldi, A. Vecchione, R. Bruzzese, S. Amoruso, Influence of ambient pressure on surface structures generated by ultrashort laser pulse irradiation, *Appl Phys A.* 124 (2018) 198. <https://doi.org/10.1007/s00339-018-1621-6>.
- [40] J. Bonse, M. Munz, H. Sturm, Structure formation on the surface of indium phosphide irradiated by femtosecond laser pulses Structure formation on the surface of indium phosphide irradiated by femtosecond laser pulses, *J Appl Phys.* 97 (2005) 013538. <https://doi.org/10.1063/1.1827919>.
- [41] J.E. Sipe, J.F. Young, J.S. Preston, H.M. van Driel, Laser-induced periodic surface structure. I. Theory, *Phys Rev* 8. 27 (1983). <https://doi.org/https://doi.org/10.1117/12.950633>.